Mapping High-Resolution Wind Fields Using Synthetic Aperture Radar

Donald R. Thompson and Robert C. Beal

The long-term goal of the research effort discussed in this article is to determine the feasibility of obtaining quantitative information about the near-surface wind field and perhaps other parameters that characterize the marine atmospheric boundary layer from an analysis of synthetic aperture radar (SAR) imagery. Because of its potential for yielding such information at high spatial resolution, this application of SAR would complement measurements from most scatterometer and passive microwave sensors that yield only coarse-resolution estimates of the wind field. Furthermore, we believe that the resulting "wind image" derived from SAR can provide a useful diagnostic tool for assessing errors in wind measurements from the coarse-resolution sensors. In this article, we discuss our initial attempts to extract high-resolution wind field maps from Radarsat imagery off the East Coast of the United States. (Keywords: High-resolution coastal winds, SAR, Synthetic aperture radar, Wind fields.)

INTRODUCTION

Wind estimates in coastal regions using conventional multiple-antenna scatterometers or passive microwave sensors are difficult to obtain because of the large footprints associated with these sensors. Synthetic aperture radar (SAR), however, can provide high-resolution imagery of the surface virtually up to the shoreline. If a realistic relationship between the backscatter cross section (suitably averaged over appropriate scales) and the surface wind vector is available, it should be possible to transform the SAR image into a wind map. Moreover, because of its high-resolution capability, SAR can resolve the surface signatures of the turbulence structure in the marine atmospheric boundary layer (MABL) (see the articles by Brown, Young, and Sikora et al., this issue). Proper characterization of this structure allows one to diagnose the surface layer stability and therefore produce wind speed estimates corrected for this important effect. Other attempts to extract wind information from SAR imagery have recently been reported by Lehner et al.[1] and Vachon and Dobson.[2]

In this article, we present a procedure for extracting high-resolution wind speed estimates from Radarsat imagery, and discuss our preliminary assessment of the utility of SAR as a high-resolution wind sensor. The imagery to be discussed in this regard is from both the Radarsat standard (100-km swath) and the wide Scan-SAR (440-km swath) beam modes. It was collected

over the Atlantic coast of the United States during the fall and winter months of 1997–1998 as part of the National Oceanic and Atmospheric Administration (NOAA) StormWatch Program. The imagery was processed by the Alaska SAR Facility (ASF). Further details of the StormWatch Program and the precise area of SAR coverage are described in the article by Beal, this issue. We first present a brief overview of conventional wind scatterometry to discuss some of the difficulties associated with this field in general and SAR scatterometry in particular. We then discuss the wind maps extracted from the SAR imagery.

CONVENTIONAL SCATTEROMETRY

It is well known that the spectral density of small-scale surface waves is a strong function of the surface wind stress. Furthermore, since the intensity of the electromagnetic field transmitted from a microwave radar and backscattered from the ocean surface is a strong function of the small-scale surface wave spectral density, it is natural to expect strong correlation between the wind stress (or wind speed) and the intensity of the backscattered radar return. Thus, it is not surprising that researchers studying scattering from the ocean concluded early on that it should be possible to measure the wind field over the ocean using microwave radars. Since the first scatterometers aboard Skylab (1973) and Seasat (1978), the construction of suitable antenna configurations as well as the development of precise algorithms for the extraction of sea surface wind fields have become important research areas.

To explain the basic ideas that govern standard scatterometer wind retrieval, we consider a simple scatterometer model function relating the normalized backscatter cross section σ_0^P (for transmit and receive polarization P) from the sea surface to the wind speed U. This function has the form

$$\sigma_0^P = aU^{\gamma}(1 + b\cos\phi + c\cos 2\phi) \ , \tag{1}$$

where ϕ is the wind direction relative to the look direction of the radar, and a, b, c, and γ are empirically determined coefficients that in general depend on the radar frequency, polarization, and incidence angle θ. One can see from Eq. 1 that σ_0^P is a monotonically increasing function of U for fixed ϕ and is symmetric about the wind direction.

Field measurements show that for moderate incidence angles ($20° \leq \theta \leq 60°$) the upwind-to-crosswind ratio is greater than the upwind-to-downwind ratio. Figure 1 shows the behavior of two popular (and significantly more complicated) scatterometer model functions. The solid curves show the model developed by Stoffelen and Anderson[3] (CMOD4), and the dashed curves show the model of Wismann.[4] The figure
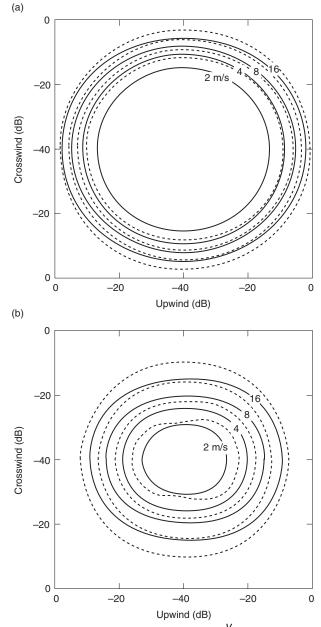

Figure 1. Normalized radar cross section, σ_0^V, with respect to wind direction for vertical polarization, incidence angles of 25° and 45° (a and b, respectively), and various wind speeds. Solid curves show the CMOD4 function, while the dashed curves show the model function of Wismann.

illustrates the angular dependence of the backscatter predicted by these models for various wind speeds and incidence angles of 25° (Fig. 1a) and 45° (Fig. 1b). Both of these models describe the backscatter cross section for the C-band (5.3 GHz) vertically polarized transmit/receive configuration characteristic of the scatterometer on the European Remote Sensing satellite (ERS-1 and -2) systems. One can see from Fig. 1 that although both models predict the same general behavior for σ_0^V, the details of the two models are rather different. The CMOD4 model will be discussed in this article because

it has received somewhat wider acceptance than that of Wismann in the conventional scatterometer community. However, uncertainties in all such models have not been completely resolved.

Although relatively well-tested algorithms such as CMOD4 exist for the C-band vertical polarization (VV) ERS-1 scatterometer, corresponding horizontal polarization (HH) models until now have not been developed. Since the Radarsat SAR operates at C-band HH, a corresponding scatterometer algorithm is required for wind field extraction using this system. We use a modification of the VV CMOD4 algorithm specifically adapted to the HH Radarsat system of the form

$$\sigma_0^H = \frac{\left(1 + \alpha \tan^2\theta\right)^2}{\left(1 + 2\tan^2\theta\right)^2}\sigma_0^V\left(U, \theta, \phi\right). \tag{2}$$

In Eq. 2, U is the wind speed, θ is the incidence angle, ϕ is the azimuth angle of the radar with respect to the wind direction, and σ_0^H and σ_0^V are the HH and VV cross sections, respectively. Further discussion of the motivation for Eq. 2 may be found in Ref. 5. Here, we note only that Eq. 2 has the interesting property that for $\alpha = 0$, σ_0^H yields the Bragg-scattering HH cross section (relative to σ_0^V), whereas for $\alpha = 1$, σ_0^H yields the Kirchhoff cross section.[6,7]

In Fig. 2, we show cross sections resulting from our hybrid HH model given by Eq. 2. The red curves show the VV cross section as a function of incidence angle for wind speeds of 4 m/s (dashed curves) and 10 m/s (solid curves) as predicted by the standard CMOD4 algorithm (with the azimuth angle $\phi = 0$). The green curves show the HH cross sections for these two wind speeds predicted using Eq. 2 with the parameter $\alpha = 0$. As noted above, with this choice of α, the polarization ratio given by Eq. 2 is that predicted by the Bragg limit. The data points at incidence angles of 20, 30, and 45° were taken from Unal et al.[8] With the α parameter in Eq. 2 set to a value of 0.6, these data are well represented by the blue curves in Fig. 2. The HH cross section given by these curves is also in reasonable agreement with those given by Campbell and Vachon.[9]

One can see from Fig. 2 that at 45°, for example, the polarization ratio (σ_0^H/σ_0^V) for both wind speeds is about -5.5 dB for $\alpha = 0.6$. We thus assume for our model that the polarization ratio is independent of wind speed. This assumption, of course, needs to be checked when more data become available. This value for the polarization ratio is significantly larger than that given by the Bragg limit or than that predicted by standard composite-type scattering models where tilt and hydrodynamic modulation effects of longer-scale waves are also included.[10] Recent scattering calculations appear to
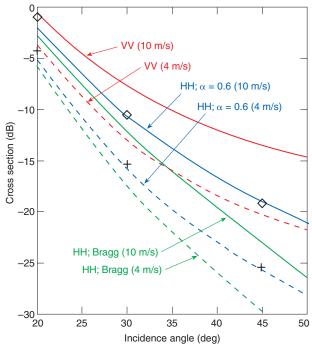

Figure 2. C-band backscatter cross section as a function of incidence angle for wind speeds of 4 and 10 m/s. The VV cross sections were computed using the CMOD4 scatterometer algorithms. The HH cross sections were computed using the expression given by Eq. 2 with $\alpha = 0.6$. The HH cross section predicted by simple Bragg scattering results from Eq. 2 when $\alpha = 0$. The data points indicated by + (4 m/s) and $\diamond$ (10 m/s) at incidence angles of 20, 30, and 45° were taken from Unal et al.[8]

indicate that the nonlinear nature of oceanic surface waves must be included in order to obtain the experimentally observed polarization ratios.[11,12] For purposes of the present study, we use the σ_0^H dependence as predicted by Eq. 2 with σ_0^V given by CMOD4. Then for particular values of θ and ϕ, and with σ_0^H specified for a particular SAR image, we can find the corresponding wind speed values by inversion.

THE WIND DIRECTION PROBLEM

As can be seen from the form of Eq. 1, an unambiguous determination of the wind direction is not possible from measurements at a single azimuth angle. In order to obtain accurate estimates of the wind vector, conventional scatterometers must view the sea surface at several different (precisely determined) azimuth angles with a footprint large enough so that a stable estimate of the cross section is obtained. For most satellite scatterometers flown to date, these requirements have been met through the use of multiple fanbeam antennas (with narrow azimuth and broad vertical beamwidths), each aligned to view the surface at well-separated azimuth angles. With this configuration, the resolution cells, where common cross-section measurements can be collected from each beam, tend to cover a rather

large expanse of the ocean surface. The ERS-1 and -2 scatterometer, for example, measures wind over a 500-km swath at a resolution of about 50 km.[13] There are three antennas on ERS-1 and -2 that illuminate approximately the same area of the surface from three different azimuth angles (±45 and 0°) with respect to the cross-flight direction at three slightly different times as the satellite moves over the area.

For SAR scatterometry, only a single look direction (usually normal to the platform velocity vector) is available. One must therefore obtain an independent estimate of the wind direction with respect to the look direction. Obtaining such an estimate of the local wind direction is one of the major difficulties that must be overcome for reliable SAR wind mapping.

Previous studies[14,15] have indicated that large-scale (kilometers) structures present in the SAR imagery, especially for unstable MABL conditions, can sometimes indicate wind direction. For example, sometimes atmospheric rolls are evident, where the axes of the rolls can be associated with the mean wind. In other cases, especially along the coast, wind shadowing is evident, and the local direction may be inferred from the location of the shadow streaks. In some instances, however, we have found that such features in SAR imagery can be almost orthogonal to the measured wind direction. Therefore, until the problem of estimating wind direction from SAR imagery is better understood, our approach is to incorporate numerical model predictions of the wind direction into our SAR wind-mapping procedure. We receive such predictions each day at 2400 UT ($\approx$1.5 h after an ascending overpass along the East Coast) and also at 1200 UT on a 1° × 1° grid over the entire globe from the Fleet Numerical Meteorological and Oceanography Center (FNMOC).

Each of the parameters required for Radarsat SAR wind extraction are now available: the relative wind azimuth ϕ is given by the FNMOC model as already noted and interpolated onto the image; the incidence angle θ is determined from the satellite geometry; and the HH cross section σ_0^H is determined from Eq. 2 using CMOD4 to compute σ_0^V. Thus, the characteristics of the high-resolution wind speed maps extracted from the imagery can be studied. We examine such maps in the following section.

HIGH-RESOLUTION WIND SPEED MAPS

Radarsat Standard Beam Imagery

In Fig. 3, we show two wind maps constructed from a Radarsat image of the East Coast just east of the mouth of the Chesapeake Bay. The SAR image used in the construction of this map was collected using the Radarsat standard beam mode from the descending segment of

orbit 10460 on 5 November 1997 at 1112 UT. The wind images span an incidence-angle range from about 24° at the right-hand edge to 30° at the left-hand edge of the scene near the coast. They are about 100 km square and have been smoothed to a pixel resolution of 150 m.
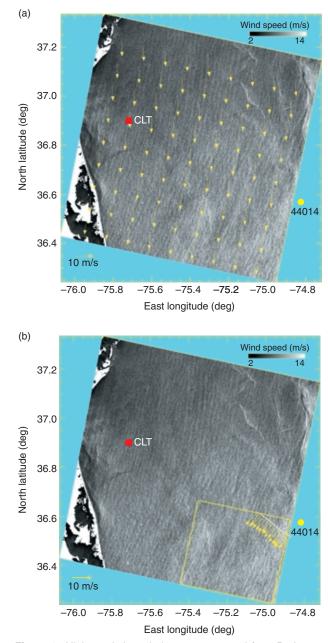

Figure 3. High-resolution wind map constructed from Radarsat standard beam, orbit 10460, just east of the mouth of the Chesapeake Bay on 5 November 1997 at 1112 UT. (a) The arrows showing the FNMOC nowcast for 1200 UT provide the wind direction estimate used in the wind extraction procedure. (b) The wind direction over the entire image was assumed to be the average direction as measured along the NOAA LongEZ flight path shown by the yellow arrows emanating from the white line in the southeastern portion of the map. The yellow box designates the wind field used in the analysis presented in the article by Mourad et al. (this issue). (CLT = Chesapeake Light Tower, 44014 = designation of the U.S. National Data Buoy Center buoy.)

The arrows superimposed on the image in Fig. 3a show the FNMOC model wind directions for 1200 UT used in the wind extraction as discussed earlier. The arrows near the lower right edge of the image in Fig. 3b show the wind direction as measured along the flight path of the NOAA LongEZ aircraft (shown by the solid white line at the base of the arrows) flying between 1203 and 1210 UT at about 15 m above the surface.[16] The statistics of the wind field enclosed by the yellow box are analyzed in detail in Mourad et al. (this issue).

The wind direction used for the wind map of Fig. 3b was chosen to be from 50°T, which is the average direction along the LongEZ flight path. (°T = degrees from true north.) The locations labeled CLT and 44014 in both images denote the position of the Chesapeake Light Tower and National Data Buoy Center (NDBC) buoy 44014, respectively. Nominal meteorological measurements are available from both of these locations, but the 44014 buoy was unfortunately not operating during the time of this SAR overpass.

Both of the wind maps in Fig. 3 have been extracted from standard beam SAR images using the inversion procedure described in the previous sections. The SAR images were smoothed to 150-m pixels before inversion. For the map in Fig. 3a, we have interpolated the FNMOC wind direction onto the 150-m pixel spacing of the smoothed SAR to specify the wind direction predictions at each pixel. Since the wind direction predictions are supplied on a $1° \times 1°$ grid, there are only about four FNMOC grid points available over the entire scene. (The arrows spaced at $\approx 0.1° \times 0.1°$ on a grid in Fig. 3a are interpolated.) The wind speed and direction measured at the CLT at 1200 UT (and corrected to neutral stability and 10 m above the surface) are 7.7 m/s from 21°T. From the wind map of Fig. 3a, we find an average wind speed from a 1.5×1.5 km^2 area centered on the CLT to be 8.0 m/s—in reasonable agreement with the CLT measurement. (The FNMOC-predicted wind direction in the vicinity of the CLT is from about 10°T.)

The wind map in Fig. 3b was constructed using the (constant) mean wind direction (from 50°T) measured along the LongEZ flight track over the entire scene. This assumption, of course, is expected to be valid only in the vicinity of the flight leg. Although they are difficult to discern from the figures, there are in fact small differences in Figs. 3a and 3b caused by the different choice of wind direction in constructing the maps.

A distinct feature seen in both images is the cellular structure oriented roughly from the top to the bottom of each of the wind maps in Fig. 3. This structure is caused by boundary-layer roll vortices caused by thermal or dynamic instabilities in the MABL as discussed elsewhere in this issue by Brown and also by Mourad[17] and Alpers.[18] Figure 4 (adapted from Fig. 6 in Alpers[18])

shows a schematic of the wind field associated with these roll vortices. This field is produced by superimposing a helical circulation pattern in the y–z plane on a mean wind vector directed along the x axis. The important point for our discussion is the variation of the near-surface wind vector across the roll as shown in Fig. 4c. This variation produces the signature in the SAR imagery. The rolls are oriented between the direction of the geostrophic wind at the top of the MABL and the direction of the surface wind (for example at 10 m). Notice that the directions of the rolls in the wind maps of Fig. 3 are not aligned with either the FNMOC or the LongEZ winds; they are right of the former and left of the latter.

In Fig. 5a, the black curve shows the running mean radar cross-sectional variation as a function of incidence angle across the SAR image in a 1.5-km-wide strip centered on the CLT. The blue curve shows the cross section predicted by our hybrid HH scatterometer model of Eq. 2 using $\alpha = 0.6$ and the wind speed and direction measured at the CLT (7.7 m/s from 21°T). The incidence angle at the CLT for this image is marked by the large brown cross in the figure at about 29.3°. The mean cross section from the image in the vicinity of the CLT is about −14.3 dB, while that predicted by our model using the measured winds is −14.5 dB, about 0.2 dB less. This small difference is due to the different wind direction from the FNMOC (used in constructing the wind map) and that measured at the CLT.

One can also see from Fig. 5a that the cross section increases for smaller incidence angles (toward the eastern edge of the image in Fig. 3a). If the FNMOC wind direction predictions, which are nearly constant along the swath centered on the CLT, are indeed correct, this

Figure 4. Atmospheric roll vortices. (a) Wind pattern associated with boundary-layer rolls, (b) vertical component of wind, and (c) horizontal component of wind. (Adapted from Fig. 6 in Alpers.[18])
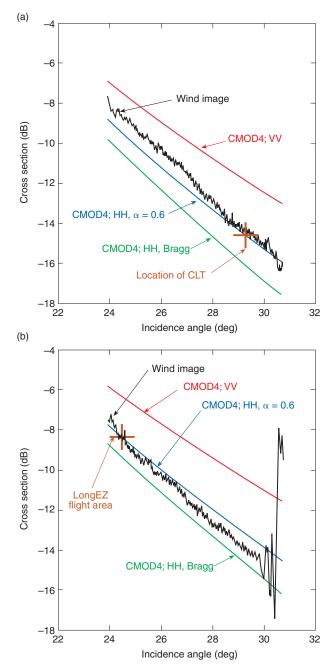
(a)

(b)

Figure 5. C-band backscatter cross section from orbit 10460 as a function of incidence angle for the conditions corresponding to (a) Fig. 3a (10 m/s neutral wind at CLT; 7.7 m/s from 21°T) and (b) Fig. 3b (10 m/s neutral wind from LongEZ; 8.1 m/s from 50°T).

increase in radar cross section (about −8.6 dB near 24.5° incidence) would correspond to a higher wind speed (about 10.5 m/s) at this position in the image. The red and green curves in Fig. 5a show the predicted cross section for VV and HH Bragg scattering, respectively. At the location of the CLT, the cross sections from these predictions are −11.8 and −16.1 dB, respectively. These cross sections correspond to wind speeds of about 14.4 and 5.2 m/s, respectively, using the hybrid HH model of Eq. 2 with α = 0.6. These numbers reflect

the sensitivity of our wind estimates to cross-sectional changes for incidence angles around 25° or so.

Figure 5b is similar to Fig. 5a, but referenced to the area under the LongEZ flight path. The black curve shows the mean cross section extracted from the image of Fig. 3b along a 1.5-km strip centered on this location. (The large cross-sectional variations in this curve beginning at about 30° indicate where the swath crosses land at the western edge of the scene, and are of course not important for the present discussion.) Again, the blue curve was computed using Eq. 2 with α = 0.6 and the mean wind speed and direction as measured aboard the LongEZ aircraft (8.1-m/s equivalent neutral wind from 50°T). The large brown cross in this figure indicates the incidence angle of the LongEZ flight area. Also as before, the red and green curves show the corresponding VV and HH Bragg cross sections, respectively.

The running mean cross sections (black curves) in Figs. 5a and b are quite similar. This, however, does not mean that the extracted wind maps also give similar wind predictions, because the wind direction of 50°T measured by the LongEZ differs by almost 30° from the 21°T wind direction measured at the CLT. This shift in wind direction means that the cross section from the SAR image near the LongEZ flight track (−8.5 dB), which yields a wind speed of about 8.1 m/s using the 50° value in Eq. 2, corresponds to a 10.5-m/s wind speed if the wind direction were from 21°T as measured at the CLT.

Wide ScanSAR Imagery

The swath width of wide ScanSAR imagery is 440 km, nearly 4.5 times as wide as the standard beam mode. Radarsat is the first and at present the only operational satellite SAR system to provide ScanSAR coverage. Such coverage is extremely important for many operational uses including high-resolution wind mapping. Because of their wide swath, however, Scan-SARs are very difficult to calibrate accurately. At the time of this writing, ASF was just beginning to provide us with reliable calibration coefficients for the Scan-SAR imagery. In the following paragraphs, we describe our attempts to achieve calibration using wind measurements from NDBC buoys. We then compare imagery calibrated in this way with that using the preliminary ASF calibration.

Lacking accurate calibration coefficients for the ScanSAR imagery, we have employed a "bootstrap" procedure. We choose a particular ScanSAR scene where there are NDBC buoys positioned at relatively uniform incidence angles across the image swath. We then determine a calibration coefficient at the position of these buoys such that the resulting cross sections yield the buoy wind speed as predicted by our hybrid scatterometer algorithm given by Eq. 2. The calibration

coefficients determined in this manner can then be used to calibrate other scenes where buoy data are not available and also to compare with scenes for which ASF calibration is provided.

The general expression specified by ASF at the time of this writing for converting the pixel value, pv, in wide ScanSAR imagery to radar cross section (σ_0^H) has the form

$$\sigma_0^H = a_2 \left[pv^2 - a_1 N(\theta) \right] + a_3 , \qquad (3)$$

where a_1, a_2, and a_3 are calibration constants and $N(\theta)$ is an incidence-angle–dependent receiver noise function. As mentioned earlier, these three constants and the noise function were not yet routinely available for ScanSAR imagery in early 1999. In lieu of this information, we assume $a_1 = a_3 = 0$ and allow for θ dependence in a_2 so that

$$\sigma_0^H = \tilde{a}_2(\theta) pv^2 . \qquad (4)$$

In Fig. 6, we show a plot of $\tilde{a}_2(\theta)$ determined using a Radarsat wide ScanSAR image collected during orbit 10710 (2230 UT, 22 November 1997) at a resolution of 300-m pixels. The points in Fig. 6 represent estimates of $\tilde{a}_2(\theta)$ determined at the incidence angle of each of the seven NDBC buoys in the scene. (The positions of the buoys labeled next to the data points in Fig. 6 are shown in the corresponding wind map in Fig. 7.) These estimates are obtained by requiring that Eq. 4 gives the cross section predicted by the scatterometer algorithm of Eq. 2 using the measured buoy wind vector. The value of pv at the buoys is taken as the average value from a 5×5 km square centered on the buoy location in the wind map in Fig. 7. The solid line in Fig. 6 shows a linear regression fit to these points. The dashed line shows the resulting expression for $\tilde{a}_2(\theta)$ if the Buzzard's Bay buoy (BUZM3) is not included. As can be seen from Fig. 6, this point appears to be an outlier, and we have found that the measured wind vectors at this (near-shore) buoy do, in fact, show larger variance than those observed at the other buoys.

Figure 7 shows the wind map constructed according to the calibration procedure defined by Eq. 4 and using the wind vectors measured at overpass time from the NDBC buoys indicated by the labeled black dots in the figure. (In extracting a wind map from this image, we used the solid line in Fig. 6 that employs all seven buoys in the calibration.) The arrows emanating from the dots at each buoy are shown with a color level to represent the measured wind speed using the same scale as the image itself. (These levels, of course, agree closely with that of the resulting wind map, as they must with our bootstrap calibration scheme, which uses the buoy wind
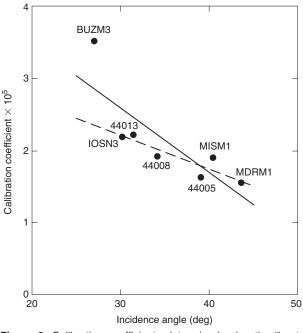

Figure 6. Calibration coefficients determined using the "bootstrap" calibration procedure based on buoy wind vectors for orbit 10710. The solid line is a linear regression using all seven buoy measurements, and the dashed line shows the fit when buoy BUZM3 is excluded.

vector to determine the calibration coefficients.) The FNMOC wind directions (arrows with no black dot in Fig. 7) are also shown in this way with their color representing the model-predicted wind speed. Note that these speeds are independent of the calibration. One can see by the visibility of the FNMOC model wind vectors against the background SAR wind field in Fig. 7 that large-scale variations in these two (independent) quantities agree well. The smaller-scale variations that are apparent in the SAR wind field are, of course, not present in the FNMOC model. A slightly different version of the wind image in Fig. 7 appears on the cover of this issue and in Beal, this issue, Fig. 5a.

The bootstrap calibration procedure was tested against other SAR scenes (assuming that the pixel values in these scenes have the same relationship to wind as in the image from orbit 10710 previously discussed). A convenient scene for such a test was collected from wide ScanSAR orbit 11396 at 2233 UT on 9 January 1998. This scene is from the 24-day repeat cycle of orbit 10710 shown in Fig. 7 (two cycles or 48 days later), and thus both scenes cover essentially the same area. Figure 8 shows the high-resolution wind map extracted from this scene using the calibration coefficients given by the solid line in Fig. 6. The NDBC buoys and FNMOC predictions are shown on the images as before. In this case, one can compare the predicted wind speed not only with the FNMOC wind speeds (as indicated by the color of the arrows), but also with the buoy-measured wind vectors, which have not
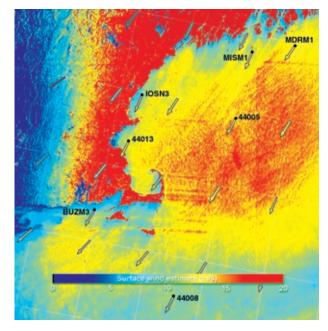
Figure 7. Wind map extracted from a Radarsat wide ScanSAR image of the New England coast during orbit 10710. The image was collected at 2230 UT on 22 November 1997. The arrows located on the grid lines in the image indicate the FNMOC wind direction at 2400 UT on 22 November 1997, and the arrows with a black dot at the tail show the wind vector at overpass time at the corresponding NDBC buoy locations. The color scale associated with both sets of arrows matches that used for the SAR wind field and reflects the speed predicted by the model or measured at the buoys.
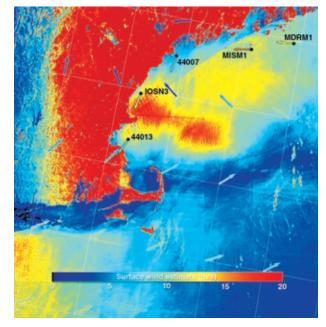

Figure 8. Wind map extracted from a Radarsat wide ScanSAR image of the New England coast during orbit 11396. The image was collected at 2233 UT on 9 January 1998. The arrows located on the grid lines in the image indicate the FNMOC wind direction at 2400 UT on 9 January 1998, and the arrows with a black dot at the tail show the wind vector at overpass time at the corresponding NDBC buoy locations. The color scale associated with both sets of arrows matches that used for the SAR wind field and reflects the speed predicted by the model or measured at the buoys.

been used in the generation of the map. These comparisons are generally favorable. The FNMOC model wind directions near the sharp frontal feature parallel to the New England coast in the center of the map do, however, show some inconsistency with the buoy wind directions since the feature is too sharp to be resolved by the model. This discrepancy can, of course, affect the extracted wind values.

One way to quantitatively assess the stability of our bootstrap calibration procedure is to repeat the process using the available NDBC buoys for orbit 11396. The calibration coefficients determined in this manner are shown by the blue dots in Fig. 9 as a function of incidence angle. For comparison, we also show the coefficients determined from orbit 10710 by the red dots. Only five NDBC buoys were operational at the time of orbit 11396 as opposed to seven during orbit 10710. Figure 9 indicates that there is a fairly tight cluster of points centered around a value of about 2×10^{-5}. Also, the MISM1 buoy is an outlier for the 11396 overpass. As was the case with the BUZM3 buoy for the 10710 overpass, we have found that the wind record from the MISM1 buoy at the time of the 11396 overpass showed a large variance. Based on these observations and the relatively close agreement of the other calibration points determined from both overpasses, we can
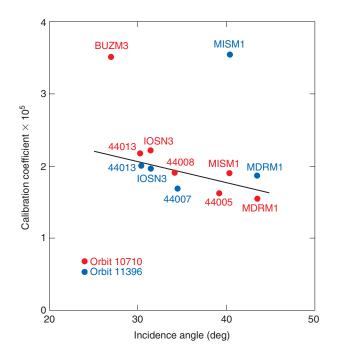

Figure 9. Calibration coefficients determined using a bootstrap calibration procedure based on buoy wind vectors from available buoys in orbits 10710 and 11396. The line is a linear regression using all buoy measurements except BUZM3 (from orbit 10710) and MISM1 (from orbit 11396).

determine a revised calibration estimate by discarding
buoys BUZM3 and MISM1 and fitting a line through
the remaining points. This revised (linear) calibration
is shown by the line in Fig. 9. It predicts a relatively
constant calibration coefficient (a change of about
30%) between the incidence angles of 25° and 45°.

The SAR image for orbit 11396, corresponding to
the wind map shown in Fig. 8, was one of the first wide
ScanSAR images supplied to us with preliminary cal-
ibration coefficients and noise function $N(\theta)$ already
determined by ASF. The existence of independent
calibration provides the opportunity for further cross-
checking. After examining the ASF coefficients, we
were immediately encouraged that the (constant) a_2
coefficient in Eq. 3 was equal to 2.2×10^{-5}. This value
is close to the mean value of our $\tilde{a}_2(\theta)$ coefficient
determined using the NDBC buoy data (Fig. 9). Fur-
thermore, the small incidence angle dependence in
$\tilde{a}_2(\theta)$ appears to compensate somewhat for neglecting
$N(\theta)$ in our calibration equation given by Eq. 4 since
this noise function becomes more important at the
higher incidence angles. (In the ASF calibration
scheme given by Eq. 3, the quantity inside the brackets
is more strongly reduced by the noise function at higher
incidence angles to yield a given cross section when
multiplied by the [constant] a_2 coefficient. In our boot-
strap calibration, Eq. 4, this same cross section can be
produced without $N(\theta)$ by a reduction in a_2 as a func-
tion of incidence angle.)

In Fig. 10, we show a scatter plot of the cross sections
computed at each of the buoy locations from orbits
10710 and 11396. We labeled only the outlier buoy
points: BUZM3 from orbit 10710 and MISM1 from
orbit 11396. The cross sections using the SAR calibra-
tion were computed using Eq. 3 with the mean pixel
values taken from a 5×5 km square centered at the
buoy location. The constants specified by ASF were
$a_1 = 1.1 \times 10^4$ and $a_2 = 2.2 \times 10^{-5}$. The noise function
for the range of incidence angles in Fig. 10 varied from
about 0.025 to 0.040. To compute the cross section
using the buoy calibration, we used Eq. 4 with $\tilde{a}_2(\theta)$
determined by the linear fit shown in Fig. 9 and the
same mean pixel values as above. It can be seen from
Fig. 10 that (except for the outlier points) the agree-
ment is reasonably good although the buoy calibration
appears to be biased somewhat high.

FUTURE PLANS

We believe that SAR has the potential to overcome
some of the inherent limitations of conventional scat-
terometry. In particular, SAR scatterometry provides
wind estimates at substantially higher resolution, allow-
ing better accuracy near strong discontinuities such as
coasts and ocean current boundaries. Furthermore,
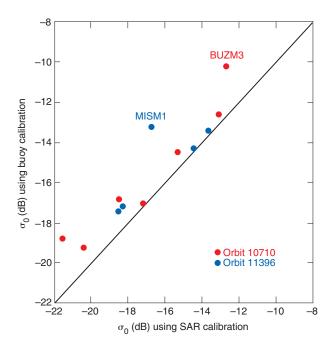since the SAR wind-extraction technique is based on

Figure 10. Scatter plot comparing the radar cross section σ_0 determined using ASF-supplied calibration coefficients and that determined using the buoy calibration procedure.

an imaging process, it is possible not only to identify
the location of these features, but also to estimate
small-scale structures in the wind field that can indicate
the atmospheric stability and possibly quantitative es-
timates of the stability parameter.

Clearly, our SAR wind-extraction procedure con-
tains errors with magnitudes depending on the fidelity
of the calibration procedure as well as the HH scatter-
ometer algorithm. The calibration issue should dimin-
ish as we begin to receive fully calibrated ScanSAR
imagery from ASF. We will, however, continue to
update our bootstrap calibration procedure using avail-
able buoy data in subsequent imagery as already dis-
cussed. The comparison of calibration coefficients de-
termined using different passes (with different wind
conditions) collected over the same region provides
useful information about the stability of the Radarsat
platform as well as the intrinsic accuracy of the cali-
bration technique. Furthermore, we will be able to
compare this bootstrap calibration with that deter-
mined by ASF when it becomes available, and assess
and improve the quality of both methods.

As noted earlier, it was necessary to develop an
approximate scatterometer algorithm that relates the
HH radar cross section measured by the Radarsat SAR
to wind speed. This task was not straightforward since
measurements indicate that the HH cross section, even
at intermediate incidence covered by the Radarsat wide
ScanSAR beam, is significantly larger than that pre-
dicted by commonly used scattering models. We are

now using the VV CMOD4 algorithm, modified for HH, to convert our Radarsat SAR imagery to wind speed. Much further testing is needed before this hybrid algorithm can be considered comparable to CMOD4. For example, we have not yet considered possible wind-vector dependence of the parameter α in Eq. 2.

In parallel with ongoing research supporting Storm-Watch, we will have access to an exciting new source of SAR imagery in the next year or so. The C-band Envisat Advanced SAR or ASAR (Attema, this issue) is now scheduled for launch by the European Space Agency late in 2000. Besides a ScanSAR mode similar to the Radarsat SAR, the Envisat ASAR will also employ an alternating polarization mode. Operating in this mode, the ASAR has the capability to collect simultaneous dual-polarization (VV and HH) images covering a wide range of incidence angles. We plan to use Envisat ScanSAR images in either VV or HH during ascending overpasses (similar to the Radarsat imagery we are now receiving for StormWatch). We also plan to use pairs of simultaneous VV and HH images using the dual-polarization mode on the corresponding descending overpasses of the same general area occurring roughly 12 h later. The dual-polarization imagery will provide a unique opportunity to study the polarization dependence of microwave backscatter from the ocean and to improve our understanding of the C-band polarization ratio. To our knowledge, such imagery with concurrent supporting buoy wind measurements has never before been available.

We believe that because of its high-resolution imaging capability, SAR scatterometry can provide a powerful complement to more conventional wind retrieval techniques. This high-resolution capability should be especially useful in littoral waters where accurate environmental monitoring is extremely important, but where many conventional remote sensing instruments are most limited. Furthermore, because of its imaging capability, SAR scatterometry can also provide a very useful diagnostic tool for assessing more standard wind retrieval techniques.

Concurrent SAR wind estimates over areas where conventional scatterometer or special sensor microwave/imager wind measurements are also available can provide high-resolution views of the ocean surface that could indicate which geophysical processes may be contributing to the surface roughness. Such knowledge could in turn be used to understand and quantify error sources in the wind estimates from the lower-resolution sensors. We are planning to test these ideas using the special sensor microwave/imager and scatterometer wind measurements concurrent with our StormWatch

Radarsat SAR imagery as well as that expected soon from Envisat.

REFERENCES

[1]Lehner, S., Horstmann, J., Koch, W., and Rosenthal, W., "Mesoscale Wind Measurements Using Recalibrated ERS SAR Images," *J. Geophys. Res.* **103**, 7847–7856 (1998).
[2]Vachon, P. W., and Dobson, F. W., "Validation of Wind Vector Retrieval from ERS-1 SAR Images Over the Ocean," *Global Atmos. Ocean Sys.* **5**, 177–187 (1996).
[3]Stoffelen, A., and Anderson, D. L. T., "Wind Retrieval and ERS-1 Scatterometer Radar Backscatter Measurements," *Adv. Space Res.* **13**, 53–60 (1993).
[4]Wismann, V., "A C-Band Scatterometer Model Derived from the Data Obtained During the ERS-1 Calibration/Validation Campaign," in *Proc. First ERS-1 Symp.*, Cannes, France, pp. 55–59 (1992).
[5]Thompson, D. R., Elfouhaily, T. M., and Chapron, B., "Polarization Ratio for Microwave Backscattering from the Ocean Surface at Low to Moderate Incidence Angles," in *1998 IEEE Int. Geosci. Remote Sens. Symp. Proc. III*, pp. 1671–1673 (1998).
[6]Elfouhaily, T., Thompson, D. R., Vandemark, D., and Chapron, B., "A New Bistatic Model for Electromagnetic Scattering from Perfectly Conducting Random Surfaces," *Waves Random Media* **9**, 281–294 (1999).
[7]Rice, S. O., "Reflection of Electromagnetic Waves from Slightly Rough Surfaces," *Commun. Appl. Math.* **4**, 351–378 (1951).
[8]Unal, C. M. H., Snooji, P., and Swart, P. J. F., "The Polarization-Dependent Relation Between Radar Backscatter from the Ocean Surface and Surface Wind Vectors at Frequencies Between 1 and 18 GHz," *IEEE Trans. Geosci. Remote Sens.* **29**, 621–626 (1991).
[9]Campbell, J. W. M., and Vachon, P. W., "Extracting Ocean Wind Vectors from Satellite Imagery," *Backscatter* **8**(2), 16–21 (1997).
[10]Romeiser, R., Alpers, W., and Wismann, V., "An Improved Composite Model for Radar Backscattering Cross Section of the Ocean Surface; 1. Theory and Model Optimization/Validation by Scatterometer Data," *J. Geophys. Res.* **102**, 25,237–25,250 (1997).
[11]Plant, W. J., "A Model for Microwave Doppler Sea Return at High Incidence Angles: Bragg Scattering from Bound, Tilted Waves," *J. Geophys. Res.* **102**, 21,131–21,146 (1997).
[12]Elfouhaily, T., Thompson, D. R., Vandemark, D., and Chapron, B., "Weakly Non-Linear Theory in EM-Bias Simulations," *J. Geophys. Res.* **104**, 7641–7647 (1999).
[13]Attema, E., "The Active Microwave Instrument On-Board the ERS-1 Satellite," *IEEE Proc.* **79**, 791–799 (1991).
[14]Gerling, T. W., "Structure of the Surface Wind Field from SeaSat SAR," *J. Geophys. Res.* **91**, 2308–2320 (1987).
[15]Fetterer, F., Gineries, D., and Wackerman, C. C., "Validating a Scatterometer Wind Algorithm for ERS-1 SAR," *IEEE Trans. Geosci. Remote Sens.* **36**, 479–492 (1997).
[16]Mourad, P., "Spatial Variability in Radar Backscatter from the Ocean Surface Imaged by Satellite-Based SAR Caused by Multiscale Atmospheric Turbulence," in *1998 IEEE Int. Geosci. Remote Sens. Symp. Proc. IV*, pp. 1941–1943 (1998).
[17]Mourad, P. D., "Viewing a Cold-Air Outbreak Using Satellite-Based Synthetic Aperture Radar and Advanced Very-High Resolution Radiometer Imagery," *J. Geophys. Res.* **101**, 16,391–16,400 (1996).
[18]Alpers, W., "Measurement of Oceanic and Atmospheric Phenomena by ERS-1 SAR," *Radio Sci. Bull.* **275**, 14–22 (1995).

THE AUTHORS

DONALD R. THOMPSON is with The Johns Hopkins University Applied Physics Laboratory, Laurel, MD. His e-mail address is donald.thompson@jhuapl.edu.

ROBERT C. BEAL is with The Johns Hopkins University Applied Physics Laboratory, Laurel, MD. His e-mail address is robert.beal@jhuapl.edu.